Chinese Chemical Letters 34 (2023) 108311

Contents lists available at ScienceDirect

Chinese Chemical Letters

journal homepage: www.elsevier.com/locate/cclet

Synthesis and properties of binaphthyl chiral thermally activated delayed fluorescence molecules using thioxanthone as acceptor

Xiangyu Dong[a,b], Shaogang Shen[a,b], Yuanyuan Qin[a,b], Xiaoxiao Hu[c], Honglei Gao[a,b], Guanhao Liu[a,b], Teng Gao[a,b], Zhi Pang[a,b], Pengfei Wang[a,b], Ying Wang[a,b,*]

[a] Key Laboratory of Photochemical Conversion and Optoelectronic Materials and CityU–CAS Joint Laboratory of Functional Materials and Devices, Technical Institute of Physics and Chemistry, Chinese Academy of Sciences, Beijing 100190, China
[b] University of Chinese Academy of Sciences, Beijing 100049, China
[c] School of Chemistry and Chemical Engineering, Suzhou University, Suzhou 234000, China

ARTICLE INFO

Article history:
Received 7 January 2023
Revised 9 February 2023
Accepted 6 March 2023
Available online 15 March 2023

Keywords:
Thermally activated delayed fluorescence
Organic light emitting diodes
Binaphthyl skeleton
Electronic circular dichroism
Circularly polarized luminescence
Thioxanthone

ABSTRACT

The currently reported axial chiral molecules based on the 3,3′-substitution of the binaphthyl skeleton are limited by intrinsic fluorescence properties, resulting in generally low device efficiencies (EQE < 5%) of related organic light emitting diodes (OLEDs). Herein, we designed and synthesized four pair of chiral binaphthyl enantiomers (*R*/*S*-**1** – *R*/*S*-**4**) adopting acceptor-donor-donor-acceptor (ADDA) structure by introducing different thioxanthone modification groups on the 3,3′-position of 2,2′-dimethoxy-1,1′-binaphthalene. Among them, emitter *R*/*S*-**2** and *R*/*S*-**4** obtained by enhancing intramolecular charge transfer exhibited TADF characteristics due to relatively small ΔE_{ST} of 0.12 eV and 0.17 eV, and relatively moderate SOC matrix elements of 0.28 cm^{-1} and 0.10 cm^{-1} between the ^{1}CT and ^{3}LE states. The CD spectra of these enantiomers in diluted solutions showed perfect mirror images and reasonable g_{abs} for small organic molecules (10^{-4}–10^{-3}). And the external quantum efficiencies (EQE) of 10.9% and 8.32% for device A and B based on emitter *S*-**2** and *S*-**4** were highest compared with currently reported axial chiral molecules based on the 3,3′-position substitution of binaphthyl skeleton, providing simple molecular design strategies to construct efficient CP-OLED device.

Organic chiral small molecules have been arousing people's interest in recent years for potential applications in three-dimensional display [1], optical spintronics [2], chiral phototransistor [3], quantum information processing [4], information encryption [5] and chiral photocatalyst [6]. Electronic circular dichroism (CD) and circularly polarized luminescence (CPL) spectroscopy have become the most widely used techniques for configurational and conformational analyses of chiral molecules. The CD spectrum is often used to study the information of the ground state chiral structure, while the CPL spectrum can help reflect the stereochemical, conformational, and three-dimensional structural information of chiral materials in the excited state [7]. Chiral luminescence molecules can directly convert unpolarized light sources into circularly polarized light, ensuring the intensity of the emitted light and simple equipment structure compared to the strategy of mechanically separating left- and right-circularly polarized light [8]. Nowadays, a series of materials possessing central chirality [9], axial chirality [10], helical chirality [11] or planar chirality [12] have been widely applied in the field of circularly polarized luminescence (CPL).

The most classical chiral 1,1′-binaphthol (BINOL) derivatives, which have both stable axial chiral configuration and electron-rich π conjugated framework, have attracted extensive attention in the field of circularly polarized organic light-emitting diodes (CP-OLEDs) construction. In 2018, Cheng *et al.* reported a pair of chiral enantiomers (*S*/*R*-**6**) containing 2,2′-dibutoxy-1,1′-binapthalene as a chiral unit and tetraphenylethene (TPE) moiety as an aggregation-induced emission (AIE) active group. The maximum external quantum efficiency (EQE_{max}) and calculated electroluminescence dissymmetry factor (g_{EL}) values are 0.48%/3.2×10^{-3} for device A (*S*-**6**) and 0.45%/-3.0×10^{-3} for device B (*R*-**6**), respectively [13]. And in 2020, they designed and synthesized blue-emission chiral enantiomers *R*-/*S*-**3** incorporating 2,2′-methylene-dioxy-1,1′-binaphthalene moieties as chiral sources and pyrene groups as fluorophores. The CP-OLEDs based on F8BT+10% *S*-**3** showed maximum external quantum efficiency of 1.40% and relatively high g_{EL} values 9.6×10^{-3} [14]. However, most of currently reported axial

* Corresponding author.
E-mail address: wangy@mail.ipc.ac.cn (Y. Wang).

https://doi.org/10.1016/j.cclet.2023.108311
1001-8417/

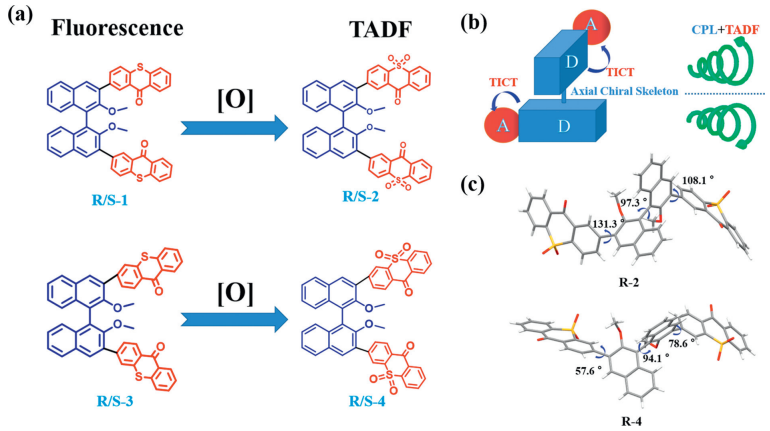

Fig. 1. (a) Chemical structures of investigated compounds *R*/*S*-**1**∼*R*/*S*-**4**. (b) Schematic diagram of molecular design strategy and (c) molecular structures in crystal of *R*-**2** and *R*-**4**.

chiral molecules based on the 3,3′-position substitution of binaphthyl skeleton can only exhibit fluorescence, and the corresponding OLED devices are generally showing low external quantum efficiencies (EQEs < 5%) due to the intrinsically inability to utilize triplet excitons under electrical excitation. In order to improve the efficiency of CP-OLEDs, thermally activated delayed fluorescence (TADF) materials have become the ideal choices due to their theoretical 100% exciton utilization [15] and diverse design concepts [16,17]. And a batch of chiral TADF molecules with high efficiency and good luminescence asymmetry factors have been developed recently [18,19].

However, most of the reported chiral TADF materials were developed by chiral perturbation strategies [18,19], which often limited the CPL properties due to the spatial separation of the TADF luminophore from the chiral unit [20]. Considering the electron-rich nature and stable axial chiral configuration of binaphthyl skeleton, it is expected to obtain a molecule with both TADF properties and intrinsic chirality when the binaphthyl donor unit is directly linked to a suitable acceptor. Thioxanthone (TX) and its derivatives have been considered as ideal acceptors for constructing efficient TADF system due to their high rate of intersystem crossing, high quantum yield of triplet formation (60%−85%) [21] and small singlet-triplet energy gap (ΔE_{ST}) [22]. In 2014, our research group designed and synthesized TXO-PhCz and TXO-TPA based on the thioxanthone unit. The OLED devices based on these two TADF molecules showed good luminescence performance with highest EQEs of 21.5% and 18.5% [23], respectively. Herein, we reported a series of chiral binaphthyl-based enantiomers (*R*/*S*-**1** to *R*/*S*-**4**, Fig. 1a) by introducing different thioxanthone modification groups on the 3,3′-position of 2,2′-dimethoxy-1,1′-binaphthalene. *R*/*S*-**1** and *R*/*S*-**3** are composed of 2-position and 3-position substituted thioxanthone units, and then oxidized to *R*/*S*-**2** and *R*/*S*-**4** to increase intramolecular charge transfer properties, respectively. This series of molecules can be regarded as an arrangement of acceptor-donor-donor-acceptor (ADDA) according to the electron withdrawing/pushing ability of molecular structural units and the assignment of conjugated units, in which the thioxanthone at the terminal position as the acceptor, and a pair of naphthyl aryl groups in the center of the molecules as the donor (Fig. 1b). Since the intramolecular charge transfer (ICT) mainly occurs between the axial chiral binaphthyl framework and thioxanthone, the emission of the excited state is expected to possess intrinsic circularly polarized emission characteristics. Among them, emitter *R*/*S*-**2** and *R*/*S*-**4** obtained by enhancing intramolecular charge transfer also exhibited TADF characteristics, and device A and B based on emitter *S*-**2** and *S*-**4** showed maximum EQE of 10.9% and 8.32%, which were highest compared with currently reported axial chiral molecules based on the 3,3′-position substitution of binaphthyl skeleton.

R/*S*-**1** to *R*/*S*-**4** were synthesized by a series of simple and scalable routes (Scheme S1 in Supporting information). We selected *R*- or *S*-binaphthol as the reaction substrate respectively, and then synthesized *R*/*S*-3,3′-diiodo-2,2′-dimethoxy-1,1′-binaphthalene according to literatures previously reported [24]. Bromo-thioxanthone units were synthesized by nucleophilic substitution, hydrolysis, and condensation with 98% concentrated sulfuric acid, and then the corresponding boronic esters were introduced *via* Suzuki-Miyaura Coupling reaction. Finally, *R*/*S*-**1** and *R*/*S*-**3** were synthesized by Pd-catalyzed Suzuki reaction with strong base barium hydroxide, and *R*/*S*-**2** and *R*/*S*-**4** were obtained by oxidation of *R*/*S*-**1** and *R*/*S*-**3** with 30% hydrogen peroxide. Their structures were fully characterized by ^{1}H NMR, ^{13}C NMR and high resolution mass spectrometry (Figs. S18-S36 in Supporting information). The thermal stability of R-**2** and *R*-**4** were measured by using thermal gravimetric analysis (TGA) and differential scanning calorimetry (DSC) under a nitrogen atmosphere (Fig. S1 in Supporting information). Both *R*-**2** and *R*-**4** exhibited excellent thermal stability with high decomposition temperature (T_d, 5% weight loss) of 435 °C and 391 °C, respectively. *R*-**2** showed high glass transition temperature (T_g) at 176 °C, and as for *R*-**4**, no obvious glass transition temperature was observed in the DCS experiment. The thermal decomposition temperature and glass transition temperature of these two compounds are relatively high among the binaphthyl derivatives, which means that the compounds can be used in the evaporation process of device preparation and ensure the normal operation of the device [25].

Single crystals of *R*-**2** and *R*-**4** were successfully grown under the condition of chloroform as good solvent and methanol as poor solvent (Fig. 1c). According to the single crystal structures, it can be seen that *R*-**2** and *R*-**4** maintain the axial chirality of the substrate *R*-binaphthol, and the dihedral angles between the two naphthyl rings are close to orthogonal (97.3°/94.1°). The torsion angles between the planes of the donor naphthyl aryl moieties and the acceptor thioxanthone reached a relatively large value in their crystals (131.3°/108.1° for *R*-**2** and 57.6°/78.6° for *R*-**4**), which greatly facilitated the efficient separation of HOMO and LUMO. Interestingly, two adjacent molecules in the dimer crystals packing exhibited absolutely different torsion angles and conformations (Fig. S2 in Supporting information). More specifically, the other molecule's twisted angles in *R*-**2** and *R*-**4** dimer crystals were 66.7°/49.2°/134.4° and 96.4°/26.4°/126.3°, respectively. Such large dihedral angles and differentially twisted conformations could prevent the formation of dentrimental species such as excimers [23].

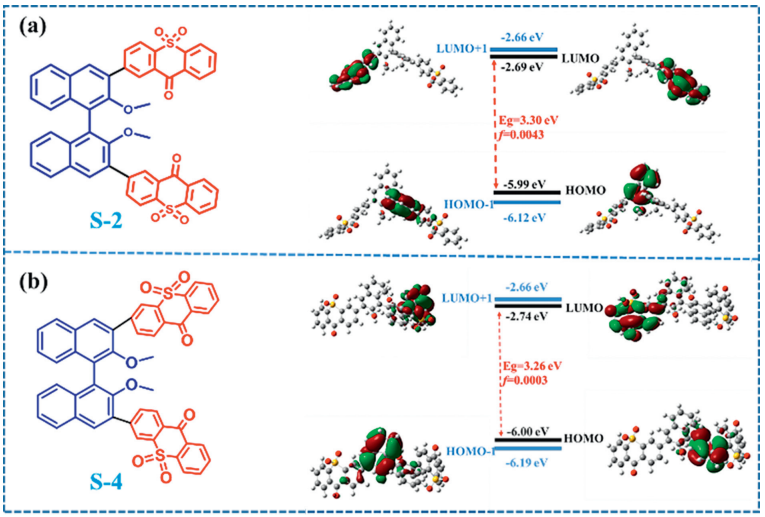

Fig. 2. The molecular structure, HOMO and LUMO electronic distributions, energy level and bandgaps (E_g) and oscillator strengths (f) of S_1 for (a) *S*-**2** and (b) *S*-**4** calculated by TD-DFT at the b3lyp/6–31 g(d,p) level.

In the dimers of *R*-**2**, the intermolecular S−O···π short contact distances between TXO units of adjacent molecules were 2.935 and 3.778 Å. And no apparent π-π interactions, which might lead to severe aggregated luminescence quenching, were observed due to the distinct conformations of these two molecules. Intermolecular C−H···π interaction with distance of 3.113 Å and S−O···π short contact with distances of 2.906 Å and 2.861 Å between TXO units could be observed in the cases of *R*-**4** dimers. All in all, there was no particularly strong interaction between adjacent molecules in dimers, but the different conformations in the dimer crystals still brought some unique photophysical phenomena, which would be discussed further later.

Density functional theory (DFT) calculations based on optimized S_0 structures at the B3LYP/6–31G(d,p) level were performed to investigate the electronic distribution and excited-state energy levels. Because the donor naphthyl aryl moieties and the acceptor oxidized thioxanthones of *S*-**2**/*S*-**4** are chemically bonded at a large torsion angle, the highest occupied molecular orbitals (HOMOs) and lowest unoccupied molecular orbital (LUMOs) of these emitters are distributed over the donor and acceptor moieties respectively (Fig. 2), resulting in a weaken exchange interaction between the HOMOs and the LUMOs and thus a small ΔE_{ST}. The electrochemical properties were determined by cyclic voltammetry in anhydrous DCM and THF solution to evaluate the HOMO and LUMO levels (Fig. S4 in Supporting information). *R*-**1** and *R*-**3** have similar HOMO levels of −5.90 eV and −5.99 eV, whereas *R*-**2** and *R*-**4** possess slightly deeper HOMO levels at −6.03 eV and −6.10 eV, respectively. At the same time, the LUMO levels of *R*-**2**/*R*-**4** at −3.39 eV/−3.45 eV are much deeper than *R*-**1**/*R*-**3** at −2.82 eV/−2.91 eV, consistent with the enhanced electron-withdrawing ability of thioxanthone upon oxidation and DFT calculated trends. According to Fermi's golden rule ($k_{RISC} \propto \langle S_1|\hat{H}_{SO}|T_1\rangle^2/\Delta E_{ST}$) [26], fast reverse intersystem crossing (RISC) could be achieved by enhancing the spin-orbit coupling (SOC) matrix element and reducing ΔE_{ST} between the excited singlet state (S_1) and triplet state (T_1) to construct efficient TADF materials [27]. Time-dependent DFT (TD-DFT) calculations for the optimized ground-state geometries were performed in order to further understand the excited states behaviors and spin-flip processes of those molecules (Fig. 3 and Fig. S5 in Supporting information). The lowest-excited S_1 for *S*-**2** and *S*-**4** (2.916 eV/2.929 eV) were dominated by the ICT transitions with obvious decrease of spatial overlap of hole and electron wavefunctions, resulting in much lower ^{1}CT energy levels compared to *S*-**1** and *S*-**3** (3.359 eV/3.486 eV). The T_1 state of *S*-**1**∼*S*-**3** (2.597 eV/2.576 eV/2.588 eV) all exhibited similar local excited features where the hole and particle were entirely localized in the vicinity of electron-donating binaphthyl moiety, and therefore showing close ^{3}LE energy levels. However, for the $^3LE_1$ state of emitter *S*-**4**, the overlaps of hole and electron density distributions extended to a small part of the oxy-thioxanthone unit in addition to the binaphthyl moiety, leading to a decrease in energy to 2.497 eV. The triplet states of these emitters were closely related to the local excited states of binaphthyl skeleton and thus exhibited close energy levels. However, the oxidized compounds *S*-**2** and *S*-**4** showed obvious ICT characteristics, which greatly reduced ^{1}CT energies, thereby reducing the ΔE_{ST}. The ΔE_{ST} values of *S*-**1**, *S*-**2**, *S*-**3** and *S*-**4** were 0.76, 0.34, 0.90 and 0.43 eV, respectively, which were much higher than the experimentally measured results but consistent with the tendency of experimental results (Fig. S8 in Supporting information). According to the El-Sayed rule [28], the obvious difference in the excitation character of the S_1 and T_1 could facilitate the spin-flip processes and contribute to the RISC processes. The calculated SOC matrix elements of *S*-**1** and *S*-**3** between the mixed hybrid local and charge-transfer (HLCT) S_1 state and local excited T_1 state achieved relatively large values of 0.55 cm^{-1} and 0.63 cm^{-1}, respectively. Despite their relatively large SOC matrix elements, *S*-**1** and *S*-**3** were unlikely to exhibit efficient reverse intersystem crossing and TADF properties due to their calculated large ΔE_{ST} of 0.76 eV and 0.90 eV. On the contrary, *S*-**2** and *S*-**4** processed much smaller calculated ΔE_{ST} of 0.34 eV and 0.43 eV and relatively moderate SOC matrix elements of 0.28 cm^{-1} and 0.10 cm^{-1} between the ^{1}CT and ^{3}LE states, which meant that *S*-**2** could manifest faster spin-flip processes and stronger TADF properties than *S*-**4** in OLED device applications.

UV−vis absorption and emission spectra were measured in dilute $CHCl_3$ solution (1×10^{-5} mol/L, 298 K) to investigate photophysical properties of these emitters (Fig. 4a and Fig. S6a in Supporting information). Compounds *R*-**1**∼*R*-**3** exhibited strong π-π^* absorption peak bands at around 290 nm, while the conjugated absorption of emitter *R*-**4** was red-shifted to 335 nm, which could be attributed to the molecular local excited (LE) absorption of binaphthyl skeleton. Broad and featureless absorptions at the bands from 350 nm to 400 nm are assigned to ICT transitions associated with electron transfer from the donor unit (binaphthyl skeleton) to acceptor 9*H*-thioxanthen-9-one or 9*H*-thioxanthen-9-one-10,10-dioxide moieties (TX or TXO). Upon photoexcitation, *R*-**1** and *R*-

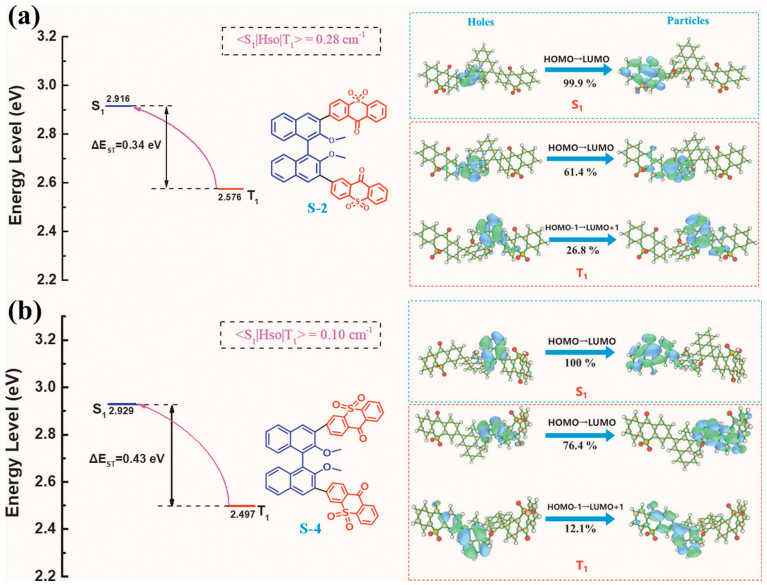

Fig. 3. Molecular structures, energy level diagrams, natural transition orbitals (NTOs) and spin-orbit coupling (SOC) matrix elements for the singlet (S_1) and triplet (T_1) excited states of (a) *S*-**2**; (b) *S*-**4**.

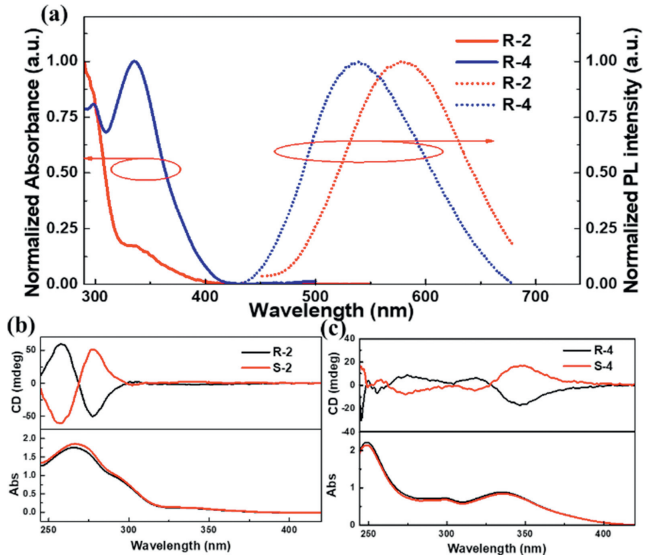

Fig. 4. (a) The normalized UV–vis and PL spectra of *R*-**2** and *R*-**4**. CD and absorption spectra of (b) *R*/*S*-**2**. (c) *R*/*S*-**4** in $CHCl_3$ solutions (1×10^{-5}) at room temperature.

3 show deep blue emission in diluted chloroform solutions with emission peaks at 428 nm and 416 nm, respectively. Meanwhile, the corresponding oxidized compounds *R*-**2** and *R*-**4** emitted orange or yellow-green light with emission peaks centered at 580 nm and 539 nm, accompanied by obvious bathochromic shift and significant reduction in emission intensity. We also noticed that this series of compounds have different degrees of red shift with the increase of solvent polarity, which further confirms that they are all typical ICT compounds (Figs. S8b-S11b in Supporting information). No obvious solvent dependence of the absorption spectra was observed for all compounds (Figs. S8a-S11a in Supporting information). ΔE_{ST} were obtained by the wavelength of the first peak of low temperature (77 K) fluorescence and phosphorescence spectra in diluted 2-MeTHF solution (Fig. S7 in Supporting information). The specific ΔE_{ST} from *R*-**1** to *R*-**4** are 0.40, 0.12, 0.45 and 0.17 eV, respectively. Enhanced electron-withdrawing ability after oxidation significantly achieves a more efficient separation of HOMO and LUMO, which effectively optimizes the energy level difference of the molecule and realizes the transformation from a fluorescent molecule to a potential TADF molecule. The photophysical parameters, frontier molecular orbital energy levels and DFT calculation results are summarized in Table S1 (Supporting information).

Transient photoluminescence (PL) decay curves of *R*-**2** and *R*-**4** doped thin films in the 1,3-bis(9*H*-carbazol-9-yl)benzene (mCP) host (5 wt%) were measured to further investigate the TADF properties and emission mechanism. The doped films exhibited green emission with emission peak at 540 nm for *R*-**2** and 550 nm for *R*-**4** (Fig. 5a) when excited at 375 nm. Both fluorophores in mCP matrix showed multi-exponential decay trend with prompt component at nanosecond-scale and delayed components at microsecond or even millisecond-scale in a vacuum environment at 300 K. *R*-**2** doped film exhibited a prompt fluorescent lifetime (τ_p) of 36.8 ns in the range of 200 ns (Fig. S13a in Supporting information), while two prompt lifetimes of 18.5/102.6 ns could be fitted for the *R*-**4** based thin film (Fig. S13b in Supporting information). The lifetime of 18.5 ns corresponded to the relaxation from S_1 to S_0 and the latter lifetime of 102.6 ns could be attributed to the interference of the delayed component causing baseline drift upward. For compound *R*-**2**, two delayed components with lifetimes (τ_d) of 21.98 μs/169.9 μs were observed inferring its RISC process at 300 K in a vacuum. And the delayed component proportion were suppressed by the oxygen in air atmosphere like most traditional TADF emitters (Fig. 5b). The delayed emission of *R*-**4** displayed much longer delayed-component lifetimes of 117.5 μs/1119 μs, and also exhibited more pronounced oxygen quenching phenomenon than emitter *R*-**2** due to the longer residence time of triplet excitons caused by larger ΔE_{ST} (Fig. 5c). As mentioned earlier, the two adjacent molecules in the dimer crystals of both *R*-**2** and *R*-**4** showed absolutely different dihedral angles and twisted conformations. Therefore, the phenomenon of double delayed components could also be attributed to the coexistence of two stable conformations which might open up two distinct emission channels for excited states. Additionally, temperature-dependent time-resolved PL decay profiles of the isomers in doped films were conducted at 300, 200 and 100 K to further investigated the photophysical properties of the delayed components (Fig. S12 in Supporting information). In the case of mCP:*R*-**2**, the lifetimes (τ_{d1} & τ_{d2}) of these two delayed components were prolonged and the propor-

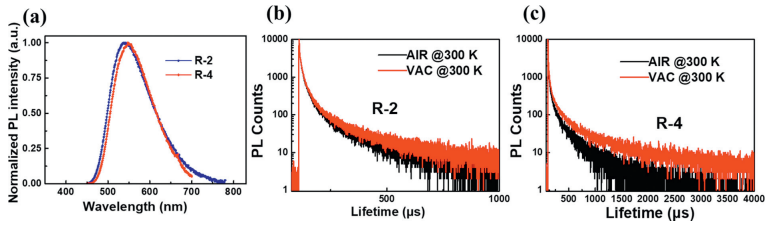

Fig. 5. (a) The normalized PL spectra of 5 wt% *R*-**2**:mCP and 5 wt% *R*-**4**:mCP films. (b) Transient PL decay curves of 5 wt% *R*-**2**:mCP film at 300 K under air and vacuum condition. (c) Transient PL decay curves of 5 wt% *R*-**4**:mCP film at 300 K under air and vacuum condition.

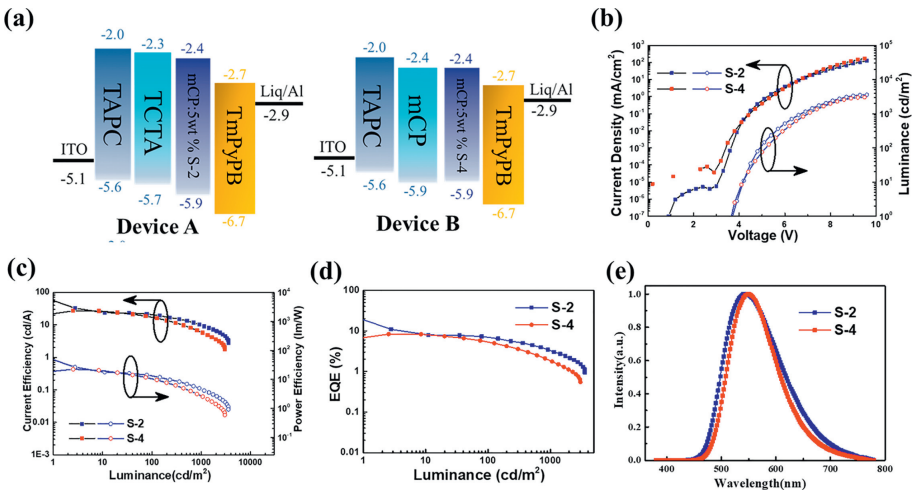

Fig. 6. (a) OLED device structures and energy levels of the materials. (b) Current density and luminance versus the voltage (*J*-*V*-*L*) characteristic. (c) Current efficiency and power efficiency versus the luminance characteristic. (d) EQE-luminance characteristic. (e) Normalized EL spectra of OLED device.

tions were also significantly reduced from 300 K to 100 K, which was in line with the trend of traditional TADF emitters exhibiting positive temperature dependence. More specifically, the overall TADF components proportion could reach 57.71%, 33.97% and 31.87% at the temperatures of 300, 200 and 100 K, respectively. As for mCP:*R*-**4**, the microsecond-scale delayed component (τ_{d1}) manifested an identical positive temperature dependence as conventional TADF emitters, and the proportion increased from 29.35% to 41.63% when the temperature rises from 100 K to 300 K. In contrast, the millisecond-scale delayed component (τ_{d2}) proportion decreased slightly from 45.54% to 37.58% when raising the temperature from 100 K to 300 K. This might be attributed to the fact that *R*-**4** can form exciplexes with mCP, but the exciplexes could not successfully equilibrate with their components [29]. And the photophysical parameters of *R*-**2** and *R*-**4** doped films were summarized in Table S2 (Supporting information). Variable temperature test results were in Tables S3 and S4 (Supporting information).

In order to investigate the ground state chiroptical properties of these enantiomers, we measured the circular dichroism (CD) spectra of *R*/*S*-**1**∼*R*/*S*-**4** in a dilute $CHCl_3$ solution (Fig. 4 and Fig. S6 in Supporting information). The CD spectra of these enantiomers showed perfect mirror images and absolutely converse Cotton effects. Among them, *R*-**1** and *R*-**2** exhibited quite similar circular dichroism trends showing positive Cotton effect in the short-wave range from 240 nm to 270 nm and negative Cotton effect between 270 nm and 350 nm, which could be attributed to the characteristic π-π^* absorption of chiral binaphthyl moieties. *R*-**3** exhibited a positive Cotton effect from 240 nm to 285 nm and a negative Cotton effect could be obtained in the range from 285 nm to 360 nm. Similar to UV−vis absorption, the overall circular dichroism spectrum of *R*/*S*-**4** is red-shifted relative to *R*/*S*-**3** accompanied by reduced CD signal at short wavelengths and enhanced CD signal at long wavelength. The largest g_{abs} values (Fig. S14 in Supporting information) for *R*/*S*-**1**, *R*/*S*-**2**, *R*/*S*-**3** and *R*/*S*-**4** are $-1.9 \times 10^{-3}/1.2 \times 10^{-3}$ (340 nm), $1.1 \times 10^{-3}/-1.1 \times 10^{-3}$ (257 nm), $-7.1 \times 10^{-4}/8.6 \times 10^{-4}$ (328 nm) and $-7.4 \times 10^{-4}/7.4 \times 10^{-4}$ (353 nm), respectively. Furthermore, CPL spectra of enantiomers were also measured in both solution (Fig. 15 in Supporting information) and thin film states (Fig. S16 in Supporting information). Unfortunately, there is no obvious CPL signal either in dilute $CHCl_3$ solution for *R*/*S*-**1**∼*R*/*S*-**4** or doped thin films in mCP host for *R*/*S*-**2** and *R*/*S*-**4**. The CPL spectra of those *R*- and *S*-enantiomers exhibited a weak mirror symmetry relationship, resulting in alternating positive and negative signals due to too weak signals and large noise. This situation has also been reported in some previous literature [30], and we plan to use polymers such as F8BT to induce chiral luminescence to enhance the CPL signal of these molecules in our future research.

Based on the sufficiently small ΔE_{ST} (0.12 eV/0.17 eV) and reasonable PL quantum yields for doped films in mCP hosts (36.9%/41.3%) of **2** and **4**, we anticipated that they would be used in efficient organic light-emitting diodes. To test their performance, we fabricated OLEDs with optimized structures for device A: ITO/1,1-bis[4-[*N*,*N*-di(tolyl)amino]phenyl]cyclohexane (TAPC) (30 nm)/4,4′,4′′-tris(carbazol-9-yl)triphenylamine (TCTA) (10 nm)/5 wt% *S*-**2**:mCP (45 nm)/1,3,5-tri[(3-pyridyl)phen-3-yl]benzene (TmPyPB) (50 nm)/8-hydroxyquinolinolato-lithium (Liq) (2 nm)/Al (100 nm), and for device B: ITO/TAPC (30 nm)/mCP (5 nm)/5 wt% *S*-**4**:mCP (20 nm)/TmPyPB (40 nm)/Liq (1 nm)/Al (100 nm), where TAPC act as the hole transport layers, TCTA and mCP act as the exciton/electron blocking layers, TmPyPB act as the electron-transport layers, Liq act as the electron-injection layers. At the doping concentration of 5 wt%, *S*-**2** device exhibited electroluminescence centered at 540 nm, while the EL spectra of *S*-**4** device is accompanied by a narrowing of full width at half

maximum and a redshift of the emission peak by 10 nm. The device A containing *S*-**2** was turned on at a voltage of 3.9 V and the current efficiency, power efficiency, EQE and maximum luminance could be up to 32.8 cd/A, 26.4 lm/W, 10.9% and 3558 cd/m^2. The device B based on *S*-**4** emitted yellow-green light with a turn-on voltage of 3.8 V, a current efficiency of 27.1 cd/A, a power efficiency of 22.4 lm/W, a slightly lower EQE of 8.32% and a maximum luminance of 3023 cd/m^2 (Fig. 6 and Table S5 in Supporting information). Considering the lower PL quantum yield of **2** relative to **4** in mCP doped films, we can attribute the higher EQE of device A compared with device B to a smaller energy level gap between S_1 and T_1 for compound **2** which promoted higher exciton utilization. More specifically, the EQEs of 10.9% and 8.32% for device A and B are equivalent to exciton utilization ratio of 98.5% and 67.2% assuming a light out-coupling efficiency of 30%.

In summary, we adopted a chiral binaphthyl skeleton to construct four pairs of novel thioxanthone derivative enantiomers, named *R*/*S*-**1**, *R*/*S*-**2**, *R*/*S*-**3** and *R*/*S*-**4**, respectively. Among them, emitter *R*/*S*-**2** and *R*/*S*-**4** obtained by enhancing intramolecular charge transfer and changing the substitution sites of thioxanthone oxide exhibited TADF characteristics as well as some unique photophysical properties, such as the opposite temperature dependence of *R*-**4** doped film. The CD spectra of these enantiomers in diluted solutions showed perfect mirror images and reasonable g_{abs} for small organic molecules (10^{-4}–10^{-3}). However, the CPL spectra of those *R*- and *S*-enantiomers exhibited a weak mirror symmetry relationship, resulting in alternating positive and negative signals due to too weak signals and large noise. And using polymers such as F8BT to induce chiral luminescence to enhance the CPL signal of those molecules will be the subject of our future research. The EQEs of 10.9% and 8.32% for device A and B based on emitter *S*-**2** and *S*-**4** were highest compared with currently reported axial chiral molecules based on the 3,3′-position substitution of binaphthyl skeleton [13,14,31], providing simple molecular design strategies to construct efficient CP-OLED device.

Declaration of competing interest

The authors declare that they have no known competing financial interests or personal relationships that could have appeared to influence the work reported in this paper.

Acknowledgments

This work was funded by National Natural Science Foundation of China (No. 21772209), International Partnership Program of Chinese Academy of Sciences (IPP) (No. 1A1111KYSB20210028) and National Program for Support of Top-notch Young Professionals.

Supplementary materials

Supplementary material associated with this article can be found, in the online version, at doi:10.1016/j.cclet.2023.108311.

References

[1] M. Schadt, Annu. Rev. Mater. Sci. 27 (1997) 305–379.
[2] R. Farshchi, M. Ramsteiner, J. Herfort, et al., Appl. Phys. Lett. 98 (2011) 162508.
[3] Y. Yang, R.C. Da Costa, M.J. Fuchter, et al., Nat. Photon. 7 (2013) 634–638.
[4] C. Wagenknecht, C.M. Li, A. Reingruber, et al., Nat. Photon. 4 (2010) 549–552.
[5] J. Shen, Q. Xiao, P. Sun, et al., ACS. Nano 15 (2021) 4947–4955.
[6] R. Alonso, T. Bach, Angew. Chem. Int. Ed. 126 (2014) 4457–4460.
[7] J.P. Riehl, F.S. Richardson, Chem. Rev. 86 (1986) 1–16.
[8] Y. Sang, J. Han, T. Zhao, P. Duan, et al., Adv. Mater. 32 (2020) 1900110.
[9] Y. Gobo, M. Yamamura, T. Nakamura, et al., Org. Lett. 18 (2016) 2719–2721.
[10] T. Kawai, K. Kawamura, H. Tsumatori, et al., ChemPhysChem 8 (2007) 1465–1468.
[11] K. Dhbaibi, L. Favereau, J. Crassous, Chem. Rev. 119 (2019) 8846–8953.
[12] M. Gon, Y. Morisaki, Y. Chujo, Chem. Commun. 53 (2017) 8304–8307.
[13] X. Zhang, Y. Zhang, H. Zhang, et al., Org. Lett. 21 (2018) 439–443.
[14] X. Zhang, Z. Xu, Y. Zhang, et al., J. Mater. Chem. C 8 (2020) 15669–15676.
[15] H. Uoyama, K. Goushi, K. Shizu, H. Nomura, C. Adachi, Nature 492 (2012) 234–238.
[16] M.Y. Wong, E. Zysman Colman, Adv. Mater. 29 (2017) 1605444.
[17] Y. Liu, C. Li, Z. Ren, S. Yan, M.R. Bryce, Nat. Rev. Mater. 3 (2018) 1–20.
[18] S. Feuillastre, M. Pauton, L. Gao, et al., J. Am. Chem. Soc. 138 (2016) 3990–3993.
[19] Z.G. Wu, H.B. Han, Z.P. Yan, et al., Adv. Mater. 31 (2019) 1900524.
[20] M. Li, Y.F. Wang, D. Zhang, et al., Angew. Chem. Int. Ed. 132 (2020) 3528–3532.
[21] M.G. Neumann, M.H. Gehlen, M.V. Encinas, et al., J. Chem. Soc. Faraday Trans. 93 (1997) 1517–1521.
[22] C. Ley, F. Morlet Savary, P. Jacques, et al., Chem. Phys. 255 (2000) 335–346.
[23] H. Wang, L. Xie, Q. Peng, et al., Adv. Mater. 26 (2014) 5198–5204.
[24] A. Minatti, K.H. Dötz, Tetrahedron: Asymmetry 16 (2005) 3256–3267.
[25] F. Song, Z. Xu, Q. Zhang, et al., Adv. Funct. Mater. 28 (2018) 1800051.
[26] V. Lawetz, G. Orlandi, W. Siebrand, J. Chem. Phys. 56 (1972) 4058–4072.
[27] P.K. Samanta, D. Kim, V. Coropceanu, et al., J. Am. Chem. Soc. 139 (2017) 4042–4051.
[28] M.A. El Sayed, J. Chem. Phys. 38 (1963) 2834–2838.
[29] X. Wei, T. Hu, Z. Li, et al., Chem. Eng. J. 433 (2022) 133546.
[30] N. Zhao, W. Gao, M. Zhang, et al., Mater. Chem. Front. 3 (2019) 1613–1618.
[31] X. Zhang, Z. Xu, Y. Zhang, et al., ACS. Appl. Mater. Interfaces 13 (2021) 55420–55427.